

Lawrence Berkeley National Laboratory

LBL Publications

Title

Visualizing Grain Statistics in MOCVD WSe₂ through Four-Dimensional Scanning Transmission Electron Microscopy

Permalink

<https://escholarship.org/uc/item/3mh0858m>

Journal

Nano Letters, 22(6)

ISSN

1530-6984

Authors

Londoño-Calderon, Alejandra

Dhall, Rohan

Ophus, Colin

et al.

Publication Date

2022-03-23

DOI

10.1021/acs.nanolett.1c04315

Copyright Information

This work is made available under the terms of a Creative Commons Attribution License, available at <https://creativecommons.org/licenses/by/4.0/>

Peer reviewed

Visualizing Grain Statistics in MOCVD WSe₂ through Four-Dimensional Scanning Transmission Electron Microscopy

Alejandra Londoño-Calderon, Rohan Dhall, Colin Ophus, Matthew Schneider, Yongqiang Wang, Enkeleda Dervishi, Hee Seong Kang, Chul-Ho Lee, Jinkyong Yoo, and Michael T. Pettes*



Cite This: *Nano Lett.* 2022, 22, 2578–2585



Read Online

ACCESS |



Metrics & More



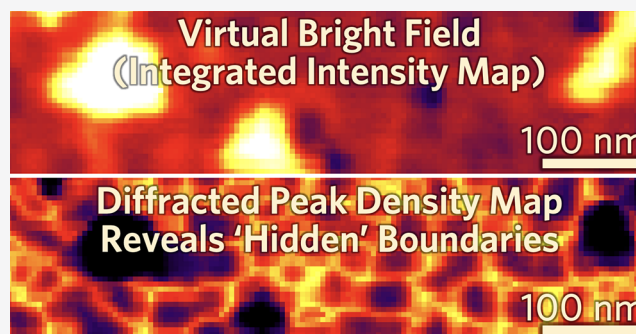
Article Recommendations



Supporting Information

ABSTRACT: Using four-dimensional scanning transmission electron microscopy, we demonstrate a method to visualize grains and grain boundaries in WSe₂ grown by metal organic chemical vapor deposition (MOCVD) directly onto silicon dioxide. Despite the chemical purity and uniform thickness and texture of the MOCVD-grown WSe₂, we observe a high density of small grains that corresponds with the overall selenium deficiency we measure through ion beam analysis. Moreover, reconstruction of grain information permits the creation of orientation maps that demonstrate the nucleation mechanism for new layers—triangular domains with the same orientation as the layer underneath induces a tensile strain increasing the lattice parameter at these sites.

KEYWORDS: 4D-STEM, 2D materials, grain boundaries, MOCVD, orientation, strain



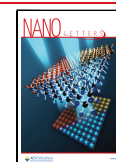
As the silicon-based industry is reaching scaling and performance limits, there has been an increasing emphasis on research into promising two-dimensional (2D) semiconducting materials, such as layered transition metal dichalcogenides (TMDs),^{1,2} in addition to new devices envisioned in the nanophotonics³ and quantum^{4–6} application spaces. For example, 2D MoS₂, WS₂, and WSe₂ are excellent candidates for room-temperature electronic, photonic, and valleytronic devices^{3,7,8} as they exhibit high photocurrent and carrier generation with the decrease in the number of layers, while retaining functionality to external fields such as strain.⁹ At present, atomically thin 2D TMDs materials for studies of fundamental physics are obtained by exfoliation from high-quality bulk crystals, or grown by the use of powder vaporization albeit with higher carrier concentrations and point defects, while the focus for industrial relevance centers on metal organic chemical vapor deposition (MOCVD).^{10,11} However, while these techniques reproduce films with high uniformity and scalability, the lateral semiepitaxial growth from each nucleation site is prone to the formation of structural defects. For example, the coalescence of grains during lateral growth results in the formation of a polycrystalline film of stitched grain boundaries (GBs) ranging from the nanometer to centimeter scale in size^{12–15} which are usually difficult to identify unless using a high-resolution imaging technique on a small portion of the lattice. Hence, the ongoing challenge has been to map grain size and intergrain misorientation angles (defined as the relative difference in the direction of in-plane lattice vector **a**) in a large field of view without altering or

destroying the sample. This characterization is vital because grains' distribution and intergrain misorientation angle strongly affect the mechanical,¹⁴ thermal,¹⁶ and electrical transport¹⁷ properties of 2D TMDs. For instance, the value of the misorientation angle at a GB can reduce the carrier mobility by several orders of magnitude.^{18–20} Therefore, understanding the extent and distribution of grains can provide fundamental insights into TMD growth mechanisms and help to optimize large-area growth methodologies for specific applications as is currently being developed for MoS₂ and WS₂.^{21,22} Since MOCVD-grown 2D materials are usually polycrystalline, one of the challenges in grain distribution analysis resides in accurately identifying the GBs over a large area. In that context, implementing lattice-sensitive techniques suitable over many length scales can be advantageous for the detection of “hidden” or “buried” grains of any size over a large field of view. For instance, four-dimensional scanning transmission electron microscopy (4D-STEM) enables the fast collection of convergent-beam/nanobeam electron diffraction (CBED/NBED) patterns on a 2D array of spatial positions²³ in which various computational analyses can reveal structural variations on a pixel-by-pixel basis over different scales while

Received: November 9, 2021

Revised: January 25, 2022

Published: February 10, 2022



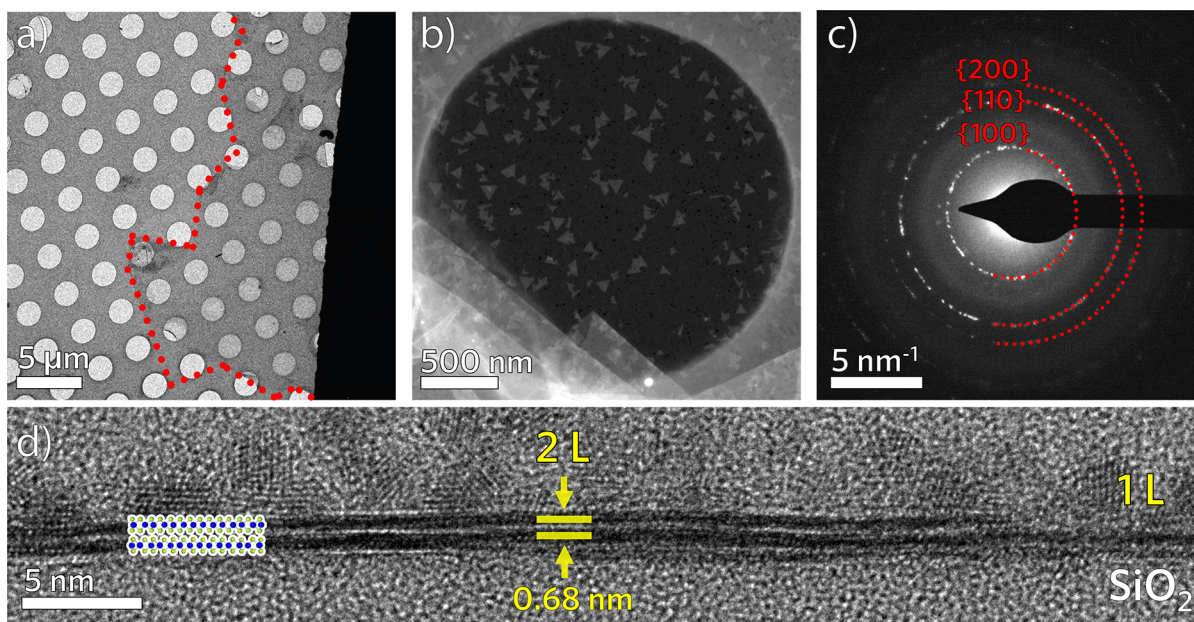


Figure 1. (a) BF-TEM image of the transferred WSe₂ film on a holey carbon grid. The red dotted line represents the sample edges. (b) HAADF-STEM image of the sample suspended over a single hole. The continuous film exhibits overgrowth, as observed by the triangular islands on top of the film. (c) Selected area electron diffraction pattern of the polycrystalline film. (d) Cross-sectional TEM image of the MOCVD-grown WSe₂ shows a thickness of one layer at the far right and two layers in the rest of the field of view.

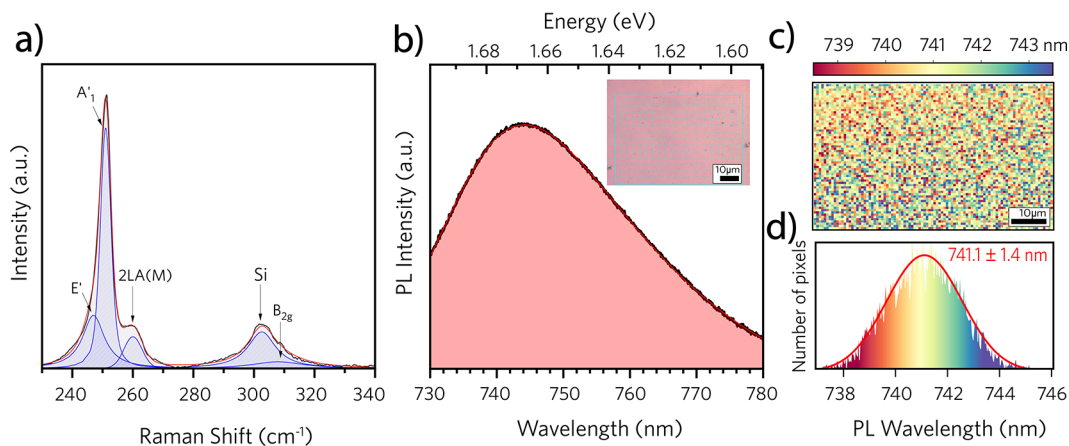


Figure 2. (a) Mean of 121 Raman spectra showing the main vibrational modes for the 1–2 layer WSe₂. (b) Mean of 5760 PL spectra showing a single asymmetric peak with a maximum at 1.67 eV. (c) Spatial map of the fitted dominant excitonic transition wavelength, and (d) histogram of the dominant peak wavelength indicate nearly homogeneous emission centered around 740 nm (single Gaussian peak, $\mu = 741.1$ nm, $\sigma = 1.4$ nm), suggesting a highly uniform film.

reducing knock-on damage in traditionally very challenging samples.^{24–26} As a result, 4D-STEM has proven to be a powerful technique for determining strain profiles, creating electrostatic maps, and generating misorientation maps for many 2D materials.^{27–32}

Here, we report the use of patterned-probe 4D-STEM to visualize the hidden grain distribution and orientation in high-purity MOCVD WSe₂ grown directly on a SiO₂ substrate. The integrated cross-correlation strength of diffracted Bragg peaks in individual NBED patterns revealed hidden grains in the film. In addition, we observed the most probably misorientation angle between grains, the spatial strain and lattice parameter profiles, and fracture mechanism through statistical analyses of the 4D-STEM data sets.

Figure 1a shows the TEM image of a WSe₂ film after transfer onto a Quantifoil TEM grid (edge of the film outlined in red

dotted line). A clean and rapid transfer of the 2D material was achieved via a sacrificial polymer³³ (details given in Supporting Information). Figure 1b shows a high-angle annular dark-field (HAADF)-STEM image of the suspended film on one of the holes of the grid. The MOCVD-grown WSe₂ consists of a continuous layer with some additional nucleated bi- or few-layer WSe₂ triangular domains which appear brighter in the HAADF scan, consistent with PL which indicated a mean thickness of 1–2 layers. The diffraction pattern in Figure 1c indicates that the layered material is highly polycrystalline like many other MOCVD-grown 2D TMDs due to the lateral growth and coalescence of grains formed in the initial stage of the growth process. The grains forming the WSe₂ film are not visible in the HAADF-STEM image in Figure 1b. Figure 1d presents a TEM image of a focused ion beam (FIB)-prepared cross-section of WSe₂ on SiO₂/Si and confirms that the sample

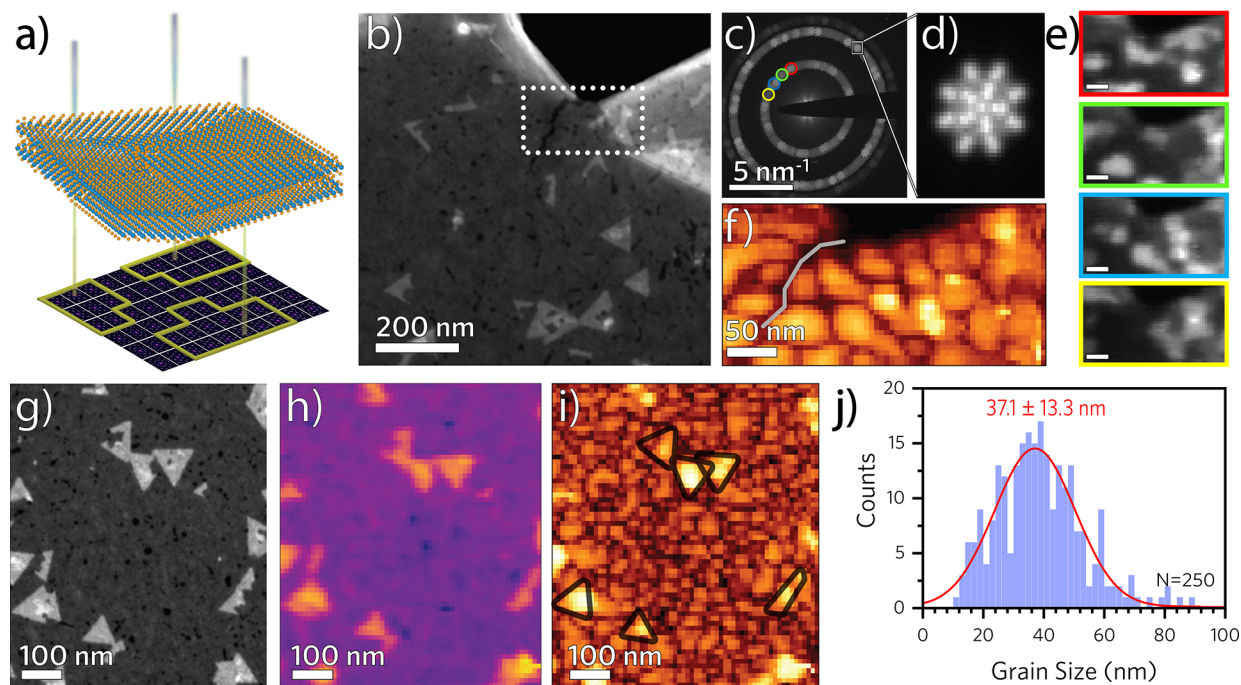


Figure 3. (a) Schematic of the 4D-STEM experiment on a 2D TMD material with GBs (highlighted in yellow). (b) HAADF-STEM image of the WSe_2 suspended over vacuum. The dotted box denotes 4D-STEM scan area. (c) Mean NBED pattern of the area in (b), and (d) patterned Bragg disk. (e) The virtual apertures in (c) produce the corresponding-color virtual images in (e), scale bar is 50 nm. (f) The diffracted peak density map reconstruction provides a faster and more reliable method to identify GBs in an arbitrary area. (g) HAADF-STEM image of a continuous area WSe_2 film, (h) 4D-STEM integrated intensity map, and (i) diffracted peak density map. Triangular overgrowth islands are marked in black lines. (j) Distribution of grain size for a population $N = 250$ gives a mean diameter of 37.1 ± 13.3 nm.

is 1–2 layers in thickness. The crystalline particles on the surface of the WSe_2 film form a thin Au layer deposited to protect the sample during the FIB cross-section preparation.

Figure 2 demonstrates the quality of the MOCVD-grown WSe_2 films obtained through confocal micro-Raman and photoluminescence (PL) spectroscopy. Figure 2a shows Raman spectrum over a $50 \times 50 \mu\text{m}^2$ area using 532 nm wavelength excitation with incident power $\sim 670 \mu\text{W}$. The instrument's response function using a reference diamond sample is described in Figure S1, Supporting Information. Accurate positions and line widths of the peaks were obtained by fixing the Gaussian component of the Voigt function to 0.83 cm^{-1} , which represents the instrumental and laser line width broadening for the experimental configuration described in the Supporting Information. Additional spectra as a function of laser power are shown in Figure S2, Supporting Information, indicating no detectable sample-heating effects. The first order semidegenerate E' and A'_1 peaks (E'_{2g} and A'_{1g} in bulk) are found at 247.00 and 251.02 cm^{-1} with intrinsic line widths of 7.40 and 3.93 cm^{-1} , respectively.^{34,35} The second-order resonant Raman mode at 260.59 cm^{-1} is related to the $2\text{LA}(\text{M})$ mode and has a line width of 4.38 cm^{-1} . The broad peak $\sim 300 \text{ cm}^{-1}$ is deconvoluted into the 302.60 cm^{-1} from the Si substrate, and the broad 307.98 cm^{-1} B_{2g} mode with line width of 14.44 cm^{-1} is associated with vibration between layers in WSe_2 .³⁶ The high intensity ratio (7.1 ± 1.9) between the $E'+A'_1$ combination mode and the $2\text{LA}(\text{M})$ mode, as well as the separation between the peaks (9.6 cm^{-1}) and the presence of the B_{2g} mode, suggest the sample averages around two layers thick.^{36–39} We note that overgrowth (bilayer) triangular crystals depicted in Figure 1b are averaged together with the monolayer film in the diffraction-limited beam diameter and so

the mean spectrum incorporates this variation in layer thickness, which is the reason for calculating statistically relevant data sets over regions hundreds-of-square-micrometers in size. Figure 2b presents the mean PL spectra obtained by mapping over a $68 \times 48 \mu\text{m}^2$ region measured with 532 nm excitation at $\sim 670 \mu\text{W}$ power. The broad peak with maximum at 743.5 nm is related to the emission of direct transition excitons.⁴⁰ Since the position and shape of the PL peak are layer dependent, the presence of a single asymmetric peak (no distinguishable shoulder) suggests the sample is 1–2 layers thick.^{38,41–43} There is no detection of defect emission at lower energies⁴⁴ as shown in the PL point spectra over a broader spectral window (Figure S3, Supporting Information). Figure 2c,d shows the spatial profile of the fitted dominant PL emission wavelength, and the corresponding histogram shows narrow distribution of emission with a maximum at $741.1 \pm 1.4 \text{ nm}$ (Gaussian 1σ). These results indicate that the high-purity MOCVD-grown WSe_2 film is homogeneous and uniform with an average thickness of 1–2 layers.

For many applications, thickness uniformity over inch-size areas is the main indicator of quality in 2D TMDs. However, controlling the formation and distribution of grains is one of the most fundamental aspects for enhancing properties, performance, and ultimately the quality of 2D-based devices. Moreover, real-space characterization of grains at the nano/atomic scale requires high-resolution techniques, for example TEM, STEM, or scanning tunneling microscopy (STM), which can only access a portion of the lattice in a small field of view; therefore, high-resolution imaging of atomic columns or individual defects in polycrystalline WSe_2 does not provide a representative analysis of the distribution of the grains in the sample. Likewise, analyzing grain distribution using conven-

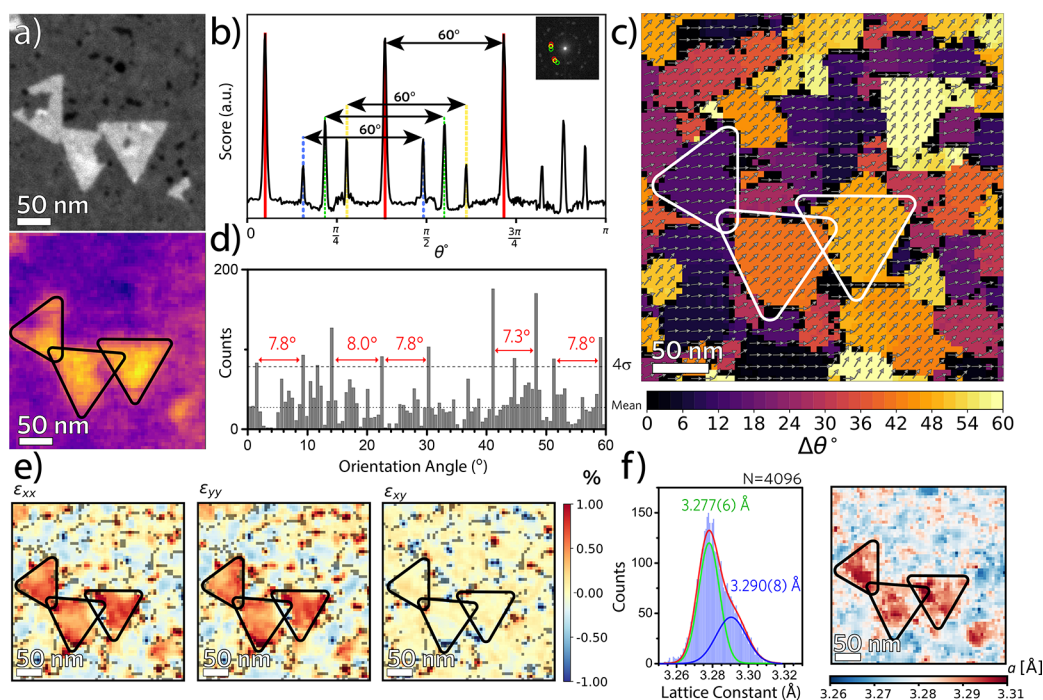


Figure 4. (a) HAADF (top) and 4D-STEM (bottom) images of suspended WSe_2 . (b) From a sinogram at each position, the total intensity or score is plotted with respect to the angular position. The most likely lattice vectors in red have the highest score. (c) Reconstruction of grains, GBs, and relative misorientation angles. (d) Histogram of orientation angles shows a most likely orientation at 41.1° and a most likely misorientation between grains of $\sim 7.8^\circ$. (e) Maps of the strain tensor components ϵ_{xx} , ϵ_{yy} , and ϵ_{xy} . (f) Distribution and map of the variation in the a lattice constant. Considerable strain and tension are observed on the triangular islands overgrowing on the film.

tional electron diffraction requires collecting a series of dark-field images^{45–49} to form a false color image. Although valid, this approach becomes a tedious task when performing statistical analyses over hundreds to thousands of grains, as is the case when the sample is composed of small stitched grains ≤ 100 nm in size. Additional methodologies to visualize GBs in 2D TMDs like selective oxidation^{50,51} and surface etching⁵² require altering the grains' pristine structure, that is, introducing artifacts in the measured size, especially for nanometer-sized grains. In contrast, 4D-STEM allows the recording of thousands of NBED patterns which permits extracting orientation information over an arbitrary field of view while causing minimum damage to the sample under controlled irradiation conditions.^{53–55}

Figure 3a shows a schematic of the 4D-STEM experiment using a custom patterned probe to enhance the disk detection in the postprocessing stage.⁵⁶ The hidden grains are defined as the array of pixels in close proximity with the same orientation, while the GBs correspond to the pixels in which there is a contribution of two or more different NBED patterns. Figure 3b shows a HAADF-STEM image of the WSe_2 film near a fracture; a 4D-STEM scan of an area of 34×32 pixels in 5 nm steps (marked in white) produces the mean NBED pattern shown in Figure 3c, composed of diffraction from a patterned probe as shown in Figure 3d. Virtual images (Figure 3e) are created by placing a virtual aperture in the spots marked in red, blue, green, and yellow on the $\{100\}$ disk and show different grains excited with each of the apertures. Hence, as we suspect a large number of grains in the 5.1×10^4 nm² area, it is not practical to find the complete set of grains in the scanned area by placing virtual apertures.

Nevertheless, since there is not significant thickness variation that can affect the intensity distribution in the patterned probe,

a reconstructed image from integrating all of the intensities at each pixel position gives a straightforward method to compare the patterns from a grain and the patterns from a GB. A comparison between the two is given in Figure S4, Supporting Information. We show the diffracted peak density map in Figure 3f (each real-space pixel is calculated as the total number of diffracted Bragg peaks) with inverted colors to make the GBs appear dark. The intensity map can detect individual grains even at the folded area on the right end (as seen on the real-space image in Figure 3b) and near the crack propagating on the MOCVD-grown WSe_2 (highlighted with a gray line). An additional example given in Figure 3g–i over a more extended area shows the HAADF-STEM real-space image, 4D-STEM integrated intensity map (each real space pixel is calculated as the sum intensity of all pixels in the corresponding NBED pattern), and the diffracted peak density map, respectively. A large number of hidden grains become visible on the intensity map from the continuous WSe_2 film. For reference, we mark the position of the triangular islands in black in Figure 3i. The grain size distribution in Figure 3j reveals a mean grain size of 37.1 ± 13.3 nm, which gives a grain density of ~ 580 grains/ μm^2 after analysis of data sets from several regions.

Once the grain distribution was obtained, we calculated the in-plane rotation angle between grains (or at the GB). The first step in 4D-STEM data analysis is to calculate the center position of all the diffraction disks at every pixel site. Using the open-source Python package py4DSTEM,⁵⁷ we can accurately detect the center of the disks by cross-correlation between the 4D-STEM data set and a reference vacuum scan of the patterned probe. The probe's particular “star” shape aids the detection and reduces error arising from intradisk features or false positives due to weak reflections.⁵⁶ We find the

orientation within a grain by measuring the angle between the first lattice vector and an arbitrarily point defined as rotation zero (along the x -axis in diffraction space). Because at the GBs several grains diffract at the same time, the orientation is then assigned to the grain with the highest intensity. In cases where the integrated intensity of several grains in a single pixel is similar, we assigned a rotation angle value of zero (black pixel) to highlight the frontiers of the GBs. Figure 4a shows the real-space HAADF-STEM image and the 4D-STEM reconstruction image, respectively. We used a small convergence semiangle for the probe (1 mrad), which leads to high-resolution in diffraction space at the expense of poor real-space resolution. Therefore, we mark the position of the top triangular domains on the 4D-STEM images for visual reference.

The pair of lattice vectors in a single crystalline domain have the same length but with the second lattice vector rotated by 60° . We calculate the pair of lattice vectors at each pixel position by performing a Radon transform on each pattern to create a sinogram of the intensity projection of the 2D array over a range of angles. For each angular position, the total intensity is considered the score. Figure 4b shows the integrated intensity of the sinogram from the pattern in the inset, where the angle between each pair of peaks with matching color is 60° ; each grain orientation is indicated in the NBED pattern on the inset. The orientation pair with the higher score (red) is the most likely lattice vector for this pixel position. All of the NBED patterns are fit by rotating the lattice vectors to the first quadrant allowing only a 0 – 60° rotation angle. Figure 4c shows the final orientation map where the discrete change in the color scale corresponds to a 2° increment. The orientation of the grains (visualized with arrows) represents the relative in-plane rotation with respect to the x -axis in the NBED patterns. Notice the area highlighted in white with a single crystalline orientation for the triangular islands and the film, meaning the second layer growing on the initial uniform WSe₂ film follows the orientation of the crystal supporting it. We note that the color scheme used here was deliberately chosen to highlight low and high angle grains, and the data plotted with a periodic color map is given in Figure S5, Supporting Information. The distribution of the relative orientation of the pixels presented in Figure 4d shows a random orientation of the grains. The most frequent orientations 4σ above the mean (dashed line) are at 14.1° , 41.1° , and 48.3° with respect to the x -axis in the NBED patterns. The most frequent relative misorientations, defined as the angular difference between grains (marked with red arrows), is 7.8° . The observed low value of the preferential misorientation angle can be a crucial factor in optimizing synthesis methodologies to enhance carrier mobility since, for example, low misorientation angles have been reported to have a stronger effect on carrier mobility than higher angle misorientations CVD-grown MoS₂.²⁰

Using the position of the lattice vectors at each pixel, Figure 4e displays maps of the components of the strain tensor ϵ_{xx} , ϵ_{yy} , and the shear ϵ_{xy} , where the color scale indicates relative changes in the strain from -1.0% (compressive) to $+1.0\%$ (tensile). We used the average position of the lattice vectors as the unstrained reference material; therefore, the calculated values are relative to the entire map. The strain's x - and y -components show a positive $\sim 1\%$ tension on the triangular islands, which we can associate with a stretch of the lattice in these new nucleation sites as they try to follow the same orientation as the grain below it. For the uniform film, we

observe tensile strain at edge areas near the GBs (represented in light black), while inside the grains, we observe a slight compressive (negative) strain of around -0.5% . On the other hand, the shear component of the strain ϵ_{xy} remains almost unstrained except for the GBs, where the random orientation of the grains caused localized positive and negative shear.

We calculated the lattice constant a for the MOCVD-grown WSe₂ by using the relation between the lattice vector for the (100) reflection and the lattice parameter a of a hexagonal crystal $q^2 = 4/(3a^2)$, the lattice parameter on each pixel position xy was calculated as the average of the N peaks detected in (100) equivalent reflections as

$$a_{xy} = \frac{2}{\sqrt{3}} \frac{1}{N} \sum_{i=1}^N \frac{1}{q_i} \quad (1)$$

Figure 4f shows the slight asymmetric distribution of a in the FOV, which can be fitted with two Gaussian functions as two preferential a values of 3.277 ± 0.006 and 3.290 ± 0.008 Å for the green and blue subpeak fits, corresponding to the film and the triangular islands, respectively. The lattice constant map is in good agreement with the strain maps, which indicate a slight compression on the uniform WSe₂ film and a tensile strain in the triangular islands and areas near a GB. Despite the relatively uniform thickness of the sample, the high density of small grains semirandomly oriented in the MOCVD-grown WSe₂ film suggests a high density of intrinsic defects produced during the synthesis. In an attempt to corroborate and quantify defects present in the sample, we used Rutherford backscattering spectrometry (RBS) to extract the stoichiometry of the MOCVD-grown WSe₂ (Figure S6, Supporting Information). The RBS results indicate a scattering yield W/Se ratio of 1:1.66, suggesting a selenium substoichiometry parameter WSe_{2-x} of $x = 0.34$. This value is considerably higher than the $x = 0.02$ ⁵⁸ and 0.08 ⁶ selenium substoichiometries obtained for different WSe₂ syntheses and is most likely a result of the high density of nucleation sites forming small ~ 37 nm grains in the wafer-scale film of this work.

The spatial resolution of 4D-STEM is limited by the need to balance the real-space resolution with the ability to clearly locate the diffraction disks in reciprocal space. Typical real-space resolution is on the order of 1.5 nm with the instrumental configuration used here. Complementary electron microscopy techniques such as traditional electron backscatter diffraction (EBSD) is not feasible with 2D materials. Transmission Kikuchi diffraction (TKD, also referred to as transmission-EBSD) may be possible with direct electron detection techniques, however conventional detectors require primary beam energies above 5 kV to enable the scattered electrons to excite the phosphor on the camera.^{28,59} At these energies the interaction between the primary electrons and the 2D material is rather weak. In order to generate the Kikuchi diffraction patterns utilized in either EBSD or TKD, the beam must undergo a number of inelastic scattering events in order to generate a spectrum of electron energies which then scatter off of the lattice planes near the exit surface. At energies greater than 5 kV, the necessary polychromatic radiation is not generated and thus these techniques are not feasible. Far-field diffraction does occur and has been utilized in other work,^{54,60} however this requires direct-transmission detection in a scanning electron microscope. In an attempt to discern even the very weak TKD signal present from our WSe₂ film (see Figure S7, Supporting Information), the data collected from

the monolayer WSe₂ showed no signs of Kikuchi diffraction, while nanoparticles of copper placed on the film as a control experiment were readily indexable. This leaves 4D-STEM as the only suitable experimental technique capable of nanoscale crystallographic characterization needed to understand the physical properties of these films.

In summary, using 4D-STEM to characterize grains and GBs by comparing the integrated intensity at each pixel is a consistent methodology that relies on intensity variations caused by the number of diffracting grains. The 1–2 layer thick film consisted of grains semirandomly oriented and with a more frequent misorientation angle of $\sim 8^\circ$. The high density of defects created a slight tensile strain at the GBs and additional layer nucleation domains. Collecting 4D data sets provides information on local orientation at each grain; hence grain size, orientation, and lattice parameters can all be analyzed from the pristine surface of MOCVD-grown WSe₂ without physical or chemical alteration of the sample. Lastly, the characterization technique developed here can play an important future role in investigations of the properties of 2D materials for a wide range of applications especially in the nanophotonics, surface coatings, and nanoelectronics areas. The structural information yielded by this investigation can serve as a useful starting point for models such as phase field calculations when predicting functionality (mechanical properties, polarizability, permeation, and so forth). With advancements in fast electron detectors and new data science techniques being applied to large diffraction data sets, we are enthusiastic that this technique will help to enable automated crystal orientation mapping (ACOM)⁶¹ in TEM in a statistically meaningful way.

■ ASSOCIATED CONTENT

SI Supporting Information

The Supporting Information is available free of charge at <https://pubs.acs.org/doi/10.1021/acs.nanolett.1c04315>.

Experimental details and additional results includes Raman calibration, Raman and PL spectra under different laser powers, NBED patterns with one-to-three grains, Rutherford backscattering spectrometry, and transmission Kikuchi diffraction (PDF)

■ AUTHOR INFORMATION

Corresponding Author

Michael T. Pettes – *Center for Integrated Nanotechnologies (CINT), Materials Physics and Applications Division, Los Alamos National Laboratory, Los Alamos, New Mexico 87545, United States*; orcid.org/0000-0001-6862-6841; Email: pettesmt@lanl.gov

Authors

Alejandra Londoño-Calderon – *Center for Integrated Nanotechnologies (CINT), Materials Physics and Applications Division, Los Alamos National Laboratory, Los Alamos, New Mexico 87545, United States*; orcid.org/0000-0002-0277-3571

Rohan Dhall – *National Center for Electron Microscopy (NCEM), Molecular Foundry, Lawrence Berkeley National Laboratory, Berkeley, California 94720, United States*

Colin Ophus – *National Center for Electron Microscopy (NCEM), Molecular Foundry, Lawrence Berkeley National Laboratory, Berkeley, California 94720, United States*

Matthew Schneider – *Materials Science in Radiation and Dynamics Extremes (MST-8), Materials Science and Technology Division, Los Alamos National Laboratory, Los Alamos, New Mexico 87545, United States*

Yongqiang Wang – *Center for Integrated Nanotechnologies (CINT), Materials Physics and Applications Division and Materials Science in Radiation and Dynamics Extremes (MST-8), Materials Science and Technology Division, Los Alamos National Laboratory, Los Alamos, New Mexico 87545, United States*

Enkeleda Dervishi – *Electrochemistry and Corrosion Team, Sigma Division, Los Alamos National Laboratory, Los Alamos, New Mexico 87545, United States*

Hee Seong Kang – *KU-KIST Graduate School of Converging Science and Technology & Department of Integrative Energy Engineering, Korea University, Seoul 02841, Republic of Korea*

Chul-Ho Lee – *KU-KIST Graduate School of Converging Science and Technology & Department of Integrative Energy Engineering, Korea University, Seoul 02841, Republic of Korea; Advanced Materials Research Division, Korea Institute of Science and Technology, Seoul 02792, Republic of Korea*; orcid.org/0000-0003-1570-8688

Jinkyung Yoo – *Center for Integrated Nanotechnologies (CINT), Materials Physics and Applications Division, Los Alamos National Laboratory, Los Alamos, New Mexico 87545, United States*; orcid.org/0000-0002-9578-6979

Complete contact information is available at:

<https://pubs.acs.org/10.1021/acs.nanolett.1c04315>

Author Contributions

M.T.P. conceived and led the project. R.D., M.T.P., A.L.-C., and C.O. performed 4D-STEM data analysis and experiment design. H.-S.K., C.-H.L., and J.Y. performed sample synthesis, M.T.P. performed optical spectroscopy, and Y.W. performed ion beam analysis. E.D. transferred the sample on a TEM grid for characterization. A.L.-C. and M.T.P. wrote the manuscript with input from all coauthors.

Notes

The authors declare no competing financial interest.

■ ACKNOWLEDGMENTS

This work was supported by the Laboratory Directed Research and Development program of Los Alamos National Laboratory under project numbers 20190516ECR, 20210036DR, 20220485MFR, and 20210782ER, and the National Security Education Center under project numbers IMS RR19PETT, IMS RR21PETT, and ISTI IP2104MP. Work at the Molecular Foundry was supported by the Office of Science, Office of Basic Energy Sciences, of the U.S. Department of Energy under Contract no. DE-AC02-05CH11231. C.O. acknowledges additional support from the Department of Energy Early Career Research Award program. C.-H.L. acknowledges support from the National Research Foundation (NRF) of Korea (2020M3D1A1110548) and the KU-KIST School Project. This work was performed in part at the Center for Integrated Nanotechnologies, an Office of Science User Facility operated for the U.S. Department of Energy (DOE) Office of Science. Los Alamos National Laboratory, an affirmative action equal opportunity employer, is managed by Triad National Security, LLC for the U.S. Department of Energy's NNSA, under contract 89233218CNA000001.

REFERENCES

- (1) Iannaccone, G.; Bonaccorso, F.; Colombo, L.; Fiori, G. Quantum engineering of transistors based on 2D materials heterostructures. *Nat. Nanotechnol.* **2018**, *13*, 183–191.
- (2) Akinwande, D.; Petrone, N.; Hone, J. Two-dimensional flexible nanoelectronics. *Nat. Commun.* **2014**, *5*, 5678.
- (3) Xia, F.; Wang, H.; Xiao, D.; Dubey, M.; Ramasubramaniam, A. Two-dimensional material nanophotonics. *Nat. Photonics* **2014**, *8*, 899–907.
- (4) Liu, X.; Hersam, M. C. 2D materials for quantum information science. *Nat. Rev. Mater.* **2019**, *4*, 669–684.
- (5) Zhao, H.; Pettes, M. T.; Zheng, Y.; Htoon, H. Site-controlled telecom-wavelength single-photon emitters in atomically-thin MoTe₂. *Nat. Commun.* **2021**, *12*, 6753.
- (6) Wu, W.; Dass, C. K.; Hendrickson, J. R.; Montañó, R. D.; Fischer, R. E.; Zhang, X.; Choudhury, T. H.; Redwing, J. M.; Wang, Y.; Pettes, M. T. Locally defined quantum emission from epitaxial few-layer tungsten diselenide. *Appl. Phys. Lett.* **2019**, *114*, 213102.
- (7) Schaibley, J. R.; Yu, H.; Clark, G.; Rivera, P.; Ross, J. S.; Seyler, K. L.; Yao, W.; Xu, X. Valleytronics in 2D materials. *Nat. Rev. Mater.* **2016**, *1*, 16055.
- (8) Desai, S. B.; Madhvapathy, S. R.; Sachid, A. B.; Llinas, J. P.; Wang, Q.; Ahn, G. H.; Pitner, G.; Kim, M. J.; Bokor, J.; Hu, C.; Wong, H.-S. P.; Javey, A. MoS₂ transistors with 1-nanometer gate lengths. *Science* **2016**, *354*, 99–102.
- (9) Dai, Z.; Liu, L.; Zhang, Z. Strain engineering of 2D materials: Issues and opportunities at the interface. *Adv. Mater.* **2019**, *31*, 1805417.
- (10) Lee, D. H.; Sim, Y.; Wang, J.; Kwon, S.-Y. Metal-organic chemical vapor deposition of 2D van der Waals materials—The challenges and the extensive future opportunities. *APL Mater.* **2020**, *8*, 030901.
- (11) Zhang, Y.; Yao, Y.; Sendeku, M. G.; Yin, L.; Zhan, X.; Wang, F.; Wang, Z.; He, J. Recent progress in CVD growth of 2D transition metal dichalcogenides and related heterostructures. *Adv. Mater.* **2019**, *31*, 1901694.
- (12) He, Y.; Tang, P.; Hu, Z.; He, Q.; Zhu, C.; Wang, L.; Zeng, Q.; Golani, P.; Gao, G.; Fu, W.; Huang, Z.; Gao, C.; Xia, J.; Wang, X.; Wang, X.; Zhu, C.; Ramasse, Q. M.; Zhang, A.; An, B.; Zhang, Y.; Martí-Sánchez, S.; Morante, J. R.; Wang, L.; Tay, B. K.; Yakobson, B. I.; Trampert, A.; Zhang, H.; Wu, M.; Wang, Q. J.; Arbiol, J.; Liu, Z. Engineering grain boundaries at the 2D limit for the hydrogen evolution reaction. *Nat. Commun.* **2020**, *11*, 57.
- (13) Jia, Z.; Hu, W.; Xiang, J.; Wen, F.; Nie, A.; Mu, C.; Zhao, Z.; Xu, B.; Tian, Y.; Liu, Z. Grain wall boundaries in centimeter-scale continuous monolayer WS₂ film grown by chemical vapor deposition. *Nanotechnology* **2018**, *29*, 255705.
- (14) Wu, J.; Cao, P.; Zhang, Z.; Ning, F.; Zheng, S.-s.; He, J.; Zhang, Z. Grain-size-controlled mechanical properties of polycrystalline monolayer MoS₂. *Nano Lett.* **2018**, *18*, 1543–1552.
- (15) Eichfeld, S. M.; Colon, V. O.; Nie, Y.; Cho, K.; Robinson, J. A. Controlling nucleation of monolayer WSe₂ during metal-organic chemical vapor deposition growth. *2D Mater.* **2016**, *3*, 025015.
- (16) Bagri, A.; Kim, S.-P.; Ruoff, R. S.; Shenoy, V. B. Thermal transport across twin grain boundaries in polycrystalline graphene from nonequilibrium molecular dynamics simulations. *Nano Lett.* **2011**, *11*, 3917–3921.
- (17) Najmaei, S.; Amani, M.; Chin, M. L.; Liu, Z.; Birdwell, A. G.; O'Regan, T. P.; Ajayan, P. M.; Dubey, M.; Lou, J. Electrical transport properties of polycrystalline monolayer molybdenum disulfide. *ACS Nano* **2014**, *8*, 7930–7937.
- (18) Park, J.; Xue, K.-H.; Mouis, M.; Triozon, F.; Cresti, A. Electron transport properties of mirror twin grain boundaries in molybdenum disulfide: Impact of disorder. *Phys. Rev. B* **2019**, *100*, 235403.
- (19) Majee, A. K.; Foss, C. J.; Aksamija, Z. Impact of mismatch angle on electronic transport across grain boundaries and interfaces in 2D materials. *Sci. Rep.* **2017**, *7*, 16597.
- (20) Ly, T. H.; Perello, D. J.; Zhao, J.; Deng, Q.; Kim, H.; Han, G. H.; Chae, S. H.; Jeong, H. Y.; Lee, Y. H. Misorientation-angle-dependent electrical transport across molybdenum disulfide grain boundaries. *Nat. Commun.* **2016**, *7*, 10426.
- (21) Chubarov, M.; Choudhury, T. H.; Hickey, D. R.; Bachu, S.; Zhang, T.; Sebastian, A.; Bansal, A.; Zhu, H.; Trainor, N.; Das, S.; Terrones, M.; Alem, N.; Redwing, J. M. Wafer-scale epitaxial growth of unidirectional WS₂ monolayers on sapphire. *ACS Nano* **2021**, *15*, 2532–2541.
- (22) Yu, H.; Liao, M.; Zhao, W.; Liu, G.; Zhou, X. J.; Wei, Z.; Xu, X.; Liu, K.; Hu, Z.; Deng, K.; Zhou, S.; Shi, J.-A.; Gu, L.; Shen, C.; Zhang, T.; Du, L.; Xie, L.; Zhu, J.; Chen, W.; Yang, R.; Shi, D.; Zhang, G. Wafer-scale growth and transfer of highly-oriented monolayer MoS₂ continuous films. *ACS Nano* **2017**, *11*, 12001–12007.
- (23) Ophus, C. Four-dimensional scanning transmission electron microscopy (4D-STEM): From scanning nanodiffraction to ptychography and beyond. *Microsc. Microanal.* **2019**, *25*, 563–582.
- (24) Bustillo, K. C.; Zeltmann, S. E.; Chen, M.; Donohue, J.; Ciston, J.; Ophus, C.; Minor, A. M. 4D-STEM of beam-sensitive materials. *Acc. Chem. Res.* **2021**, *54*, 2543–2551.
- (25) Wen, Y.; Ophus, C.; Allen, C. S.; Fang, S.; Chen, J.; Kaxiras, E.; Kirkland, A. I.; Warner, J. H. Simultaneous identification of low and high atomic number atoms in monolayer 2D materials using 4D scanning transmission electron microscopy. *Nano Lett.* **2019**, *19*, 6482–6491.
- (26) Gallagher-Jones, M.; Ophus, C.; Bustillo, K. C.; Boyer, D. R.; Panova, O.; Glynn, C.; Zee, C.-T.; Ciston, J.; Mancina, K. C.; Minor, A. M.; Rodriguez, J. A. Nanoscale mosaicity revealed in peptide microcrystals by scanning electron nanodiffraction. *Commun. Biol.* **2019**, *2*, 26.
- (27) Psilodimitrakopoulos, S.; Orekhov, A.; Mouchliadis, L.; Jannis, D.; Maragkakis, G. M.; Kourmoulakis, G.; Gauquelin, N.; Kioseoglou, G.; Verbeeck, J.; Stratakis, E. Optical versus electron diffraction imaging of twist-angle in 2D transition metal dichalcogenide bilayer superlattices. **2021**, 2104.05783. arXiv. <https://arxiv.org/abs/2104.05783> (accessed August 14, 2021).
- (28) Londoño-Calderon, A.; Williams, D. J.; Schneider, M. M.; Savitzky, B. H.; Ophus, C.; Pettes, M. T. Local lattice deformation of tellurene grain boundaries by four-dimensional electron microscopy. *J. Phys. Chem. C* **2021**, *125*, 3396–3405.
- (29) Kazmierczak, N. P.; Van Winkle, M.; Ophus, C.; Bustillo, K. C.; Carr, S.; Brown, H. G.; Ciston, J.; Taniguchi, T.; Watanabe, K.; Bediako, D. K. Strain fields in twisted bilayer graphene. *Nat. Mater.* **2021**, *20*, 956–963.
- (30) Londoño-Calderon, A.; Williams, D. J.; Ophus, C.; Pettes, M. T. 1D to 2D transition in tellurium observed by 4D electron microscopy. *Small* **2020**, *16*, 2005447.
- (31) Fang, S.; Wen, Y.; Allen, C. S.; Ophus, C.; Han, G. G. D.; Kirkland, A. I.; Kaxiras, E.; Warner, J. H. Atomic electrostatic maps of 1D channels in 2D semiconductors using 4D scanning transmission electron microscopy. *Nat. Commun.* **2019**, *10*, 1127.
- (32) Han, Y.; Nguyen, K.; Cao, M.; Cueva, P.; Xie, S.; Tate, M. W.; Purohit, P.; Gruner, S. M.; Park, J.; Muller, D. A. Strain mapping of two-dimensional heterostructures with subpicometer precision. *Nano Lett.* **2018**, *18*, 3746–3751.
- (33) Aucter, E.; Marquez, J.; Yarbrow, S. L.; Dervishi, E. A facile alternative technique for large-area graphene transfer via sacrificial polymer. *AIP Adv.* **2017**, *7*, 125306.
- (34) del Corro, E.; Botello-Méndez, A.; Gillet, Y.; Elias, A. L.; Terrones, H.; Feng, S.; Fantini, C.; Rhodes, D.; Pradhan, N.; Balicas, L.; Gonze, X.; Charlier, J. C.; Terrones, M.; Pimenta, M. A. Atypical exciton–phonon interactions in WS₂ and WSe₂ monolayers revealed by resonance Raman spectroscopy. *Nano Lett.* **2016**, *16*, 2363–2368.
- (35) Zhao, W.; Ghorannevis, Z.; Amara, K. K.; Pang, J. R.; Toh, M.; Zhang, X.; Kloc, C.; Tan, P. H.; Eda, G. Lattice dynamics in mono- and few-layer sheets of WS₂ and WSe₂. *Nanoscale* **2013**, *5*, 9677–9683.
- (36) O'Brien, M.; McEvoy, N.; Hanlon, D.; Hallam, T.; Coleman, J. N.; Duesberg, G. S. Mapping of low-frequency Raman modes in CVD-grown transition metal dichalcogenides: Layer number, stacking orientation and resonant effects. *Sci. Rep.* **2016**, *6*, 19476.

- (37) Terrones, H.; Corro, E. D.; Feng, S.; Poumirol, J. M.; Rhodes, D.; Smirnov, D.; Pradhan, N. R.; Lin, Z.; Nguyen, M. A. T.; Elías, A. L.; Mallouk, T. E.; Balicas, L.; Pimenta, M. A.; Terrones, M. New first order Raman-active modes in few layered transition metal dichalcogenides. *Sci. Rep.* **2015**, *4*, 4215.
- (38) Huang, J.-K.; Pu, J.; Hsu, C.-L.; Chiu, M.-H.; Juang, Z.-Y.; Chang, Y.-H.; Chang, W.-H.; Iwasa, Y.; Takenobu, T.; Li, L.-J. Large-area synthesis of highly crystalline WSe₂ monolayers and device applications. *ACS Nano* **2014**, *8*, 923–930.
- (39) Sahin, H.; Tongay, S.; Horzum, S.; Fan, W.; Zhou, J.; Li, J.; Wu, J.; Peeters, F. M. Anomalous Raman spectra and thickness-dependent electronic properties of WSe₂. *Phys. Rev. B* **2013**, *87*, 165409.
- (40) Liu, Y.; Li, H.; Qiu, C.; Hu, X.; Liu, D. Layer-dependent signatures for exciton dynamics in monolayer and multilayer WSe₂ revealed by fluorescence lifetime imaging measurement. *Nano Res.* **2020**, *13*, 661–666.
- (41) Zeng, H.; Liu, G.-B.; Dai, J.; Yan, Y.; Zhu, B.; He, R.; Xie, L.; Xu, S.; Chen, X.; Yao, W.; Cui, X. Optical signature of symmetry variations and spin-valley coupling in atomically thin tungsten dichalcogenides. *Sci. Rep.* **2013**, *3*, 1608.
- (42) Tonndorf, P.; Schmidt, R.; Böttger, P.; Zhang, X.; Börner, J.; Liebig, A.; Albrecht, M.; Kloc, C.; Gordan, O.; Zahn, D. R. T.; Michaelis de Vasconcelos, S.; Bratschitsch, R. Photoluminescence emission and Raman response of monolayer MoS₂, MoSe₂, and WSe₂. *Opt. Express* **2013**, *21*, 4908–4916.
- (43) Zhao, W.; Ghorannevis, Z.; Chu, L.; Toh, M.; Kloc, C.; Tan, P.-H.; Eda, G. Evolution of electronic structure in atomically thin sheets of WS₂ and WSe₂. *ACS Nano* **2013**, *7*, 791–797.
- (44) Zhao, S.; Tao, L.; Miao, P.; Wang, X.; Liu, Z.; Wang, Y.; Li, B.; Sui, Y.; Wang, Y. Strong room-temperature emission from defect states in CVD-grown WSe₂ nanosheets. *Nano Res.* **2018**, *11*, 3922–3930.
- (45) Lee, G.-H.; Cooper, R. C.; An, S. J.; Lee, S.; van der Zande, A.; Petrone, N.; Hammerberg, A. G.; Lee, C.; Crawford, B.; Oliver, W.; Kysar, J. W.; Hone, J. High-strength chemical-vapor-deposited graphene and grain boundaries. *Science* **2013**, *340*, 1073–1076.
- (46) van der Zande, A. M.; Huang, P. Y.; Chenet, D. A.; Berkelbach, T. C.; You, Y.; Lee, G.-H.; Heinz, T. F.; Reichman, D. R.; Muller, D. A.; Hone, J. C. Grains and grain boundaries in highly crystalline monolayer molybdenum disulphide. *Nat. Mater.* **2013**, *12*, 554–561.
- (47) Najmaei, S.; Liu, Z.; Zhou, W.; Zou, X.; Shi, G.; Lei, S.; Yakobson, B. I.; Idrobo, J.-C.; Ajayan, P. M.; Lou, J. Vapour phase growth and grain boundary structure of molybdenum disulphide atomic layers. *Nat. Mater.* **2013**, *12*, 754–759.
- (48) Kim, K.; Lee, Z.; Regan, W.; Kisielowski, C.; Crommie, M. F.; Zettl, A. Grain boundary mapping in polycrystalline graphene. *ACS Nano* **2011**, *5*, 2142–2146.
- (49) Huang, P. Y.; Ruiz-Vargas, C. S.; van der Zande, A. M.; Whitney, W. S.; Levendorf, M. P.; Kevek, J. W.; Garg, S.; Alden, J. S.; Hustedt, C. J.; Zhu, Y.; Park, J.; McEuen, P. L.; Muller, D. A. Grains and grain boundaries in single-layer graphene atomic patchwork quilts. *Nature* **2011**, *469*, 389–392.
- (50) Lee, J.-Y.; Lee, J.-H.; Kim, M. J.; Dash, J. K.; Lee, C.-H.; Joshi, R.; Lee, S.; Hone, J.; Soon, A.; Lee, G.-H. Direct observation of grain boundaries in chemical vapor deposited graphene. *Carbon* **2017**, *115*, 147–153.
- (51) Ly, T. H.; Chiu, M.-H.; Li, M.-Y.; Zhao, J.; Perello, D. J.; Cichocka, M. O.; Oh, H. M.; Chae, S. H.; Jeong, H. Y.; Yao, F.; Li, L.-J.; Lee, Y. H. Observing grain boundaries in CVD-grown monolayer transition metal dichalcogenides. *ACS Nano* **2014**, *8*, 11401–11408.
- (52) Wang, J.; Xu, X.; Qiao, R.; Liang, J.; Liu, C.; Zheng, B.; Liu, L.; Gao, P.; Jiao, Q.; Yu, D.; Zhao, Y.; Liu, K. Visualizing grain boundaries in monolayer MoSe₂ using mild H₂O vapor etching. *Nano Res.* **2018**, *11*, 4082–4089.
- (53) Nalin Mehta, A.; Gauquelin, N.; Nord, M.; Orekhov, A.; Bender, H.; Cerbu, D.; Verbeeck, J.; Vandervorst, W. Unravelling stacking order in epitaxial bilayer MX₂ using 4D-STEM with unsupervised learning. *Nanotechnology* **2020**, *31*, 445702.
- (54) Caplins, B. W.; Holm, J. D.; White, R. M.; Keller, R. R. Orientation mapping of graphene using 4D STEM-in-SEM. *Ultramicroscopy* **2020**, *219*, 113137.
- (55) Shevitski, B.; Chen, C. T.; Kastl, C.; Kuykendall, T.; Schwartzberg, A.; Aloni, S.; Zettl, A. Characterizing transition-metal dichalcogenide thin-films using hyperspectral imaging and machine learning. *Sci. Rep.* **2020**, *10*, 11602.
- (56) Zeltmann, S. E.; Müller, A.; Bustillo, K. C.; Savitzky, B.; Hughes, L.; Minor, A. M.; Ophus, C. Patterned probes for high precision 4D-STEM Bragg measurements. *Ultramicroscopy* **2020**, *209*, 112890.
- (57) Savitzky, B. H.; Zeltmann, S. E.; Hughes, L. A.; Brown, H. G.; Zhao, S.; Pelz, P. M.; Pekin, T. C.; Barnard, E. S.; Donohue, J.; DaCosta, L. R.; Kennedy, E.; Xie, Y.; Janish, M. T.; Schneider, M. M.; Herring, P.; Gopal, C.; Anapolsky, A.; Dhall, R.; Bustillo, K. C.; Ercius, P.; Scott, M. C.; Ciston, J.; Minor, A. M.; Ophus, C. py4DSTEM: A software package for four-dimensional scanning transmission electron microscopy data analysis. *Microsc. Microanal.* **2021**, *27*, 712–743.
- (58) Wu, W.; Morales-Acosta, M. D.; Wang, Y.; Pettes, M. T. Isotope effect in bilayer WSe₂. *Nano Lett.* **2019**, *19*, 1527–1533.
- (59) Londoño-Calderon, A.; Williams, D. J.; Schneider, M. M.; Savitzky, B. H.; Ophus, C.; Ma, S.; Zhu, H.; Pettes, M. T. Intrinsic helical twist and chirality in ultrathin tellurium nanowires. *Nanoscale* **2021**, *13*, 9606–9614.
- (60) Orekhov, A.; Jannis, D.; Gauquelin, N.; Guzzinati, G.; Nalin Mehta, A.; Psilodimitrakopoulos, S.; Mouchliadis, L.; Sahoo, P. K.; Paradisanos, I.; Ferrari, A. C.; Kioseoglou, G.; Stratakis, E.; Verbeeck, J. Wide field of view crystal orientation mapping of layered materials. *2020*, 2011.01875. arXiv. <https://arxiv.org/abs/2011.01875> (accessed January 13, 2022).
- (61) Ophus, C.; Zeltmann, S. E.; Bruefach, A.; Rakowski, A.; Savitzky, B. H.; Minor, A. M.; Scott, M. C. Automated crystal orientation mapping in py4DSTEM using sparse correlation matching. *2021*, 2111.00171. arXiv. <https://arxiv.org/abs/2111.00171> (accessed January 10, 2022).